



## Phonon-induced contrast in a matter-wave interferometer

Qian Xiang <sup>1</sup>, Run Zhou <sup>1</sup>, Sougato Bose,<sup>2</sup> and Anupam Mazumdar<sup>1</sup>

<sup>1</sup>*Van Swinderen Institute, University of Groningen, 9747 AG, The Netherlands*

<sup>2</sup>*Department of Physics and Astronomy, University College London, Gower Street, WC1E 6BT London, United Kingdom*



(Received 22 April 2024; accepted 24 September 2024; published 15 October 2024)

Utilizing the Stern-Gerlach apparatus to create matter-wave superposition states is a long-sought-after goal, not only due to its potential applications in the quantum realm, but also because of its fundamental implications for studying the quantum properties of gravity. The main challenge in creating a macroscopic quantum interferometer arises from the loss of coherence, primarily through two channels. One channel involves strong coupling with the environment for macroscopic matter, leading to decoherence. The other channel relates to the precision of wave-packet overlap, which can occur due to external and internal fluctuations of various sources. The latter introduces a unique challenge for larger-scale masses by perturbing the center of mass motion of the macroscopic object. Here we study a particular challenge, namely, the issue of internal degrees of freedom, specifically phonon fluctuations and contrast reduction. This work investigates the contrast reduction caused by spin-magnetic-field-phonon and diamagnetism-phonon interactions in the quantum gravity-induced entanglement of masses protocol configuration.

DOI: [10.1103/PhysRevA.110.042614](https://doi.org/10.1103/PhysRevA.110.042614)

### I. INTRODUCTION

The matter-wave interferometer is an essential tool for generating sizable spatial superposition states. It represents the forefront of theoretical physics, as the creation of spatial superposition states can aid in constructing a theory that reconciles gravity with quantum mechanics [1–5] and studying the equivalence principle [6–9] and the decoherence mechanism [10–21]. In terms of applications, matter-wave interferometers are also considered for detecting gravitational waves [22], neutrinos [23], and light axionlike particles [24]; precise measurements of earth’s gravitational acceleration [22,25–32]; and detection of space debris [33].

To test the quantum nature of gravity, a proposal known as quantum-gravity-induced entanglement of masses (QGEM) has been proposed [34]. To further probe the nature of gravity, the gravitational-optomechanical test, which tests the analog of the light-bending experiment in quantum gravity [35], and measurement-based tests [36] require the creation of a matter-wave interferometer.

The QGEM proposal utilizes two masses, each prepared in a spatial superposition state, which is kept at a distance where the only interaction between them is mediated via gravity. Suppose detectable entanglement exists between these two masses. In that case, one can ascertain that the gravitational interaction is quantum in nature [37–43]. This quantum-entanglement-based experiment is concordant with the local operations and classical communication theorem, which states that classically one cannot mediate quantum entanglement between two quantum systems [44].

In QGEM, the spatial superposition is created by the Stern-Gerlach (SG) apparatus [45]. At the same time, the test mass is a diamond internally embedded with a nitrogen-vacancy (NV) center. The SG device utilizes the coupling between the magnetic field and the spin (NV center) to create a

spatial superposition state. Based on similar mechanisms, there have been approaches toward atom interferometry. Such an interferometer has been experimentally realized on atom chips for half-loop [46] and full-loop [47] schemes. For the former, the coherent time for maintaining spatial superposition was 21.45 ms, and the size of 3.98  $\mu\text{m}$  was reached. For the full loop, the coherent time and superposition size were 7 ms and 0.38  $\mu\text{m}$ , respectively.

Of course, QGEM imposes higher demands on the interferometer’s performance, with critical requirements including the diamond’s mass  $M \sim 10^{-15}$ – $10^{-14}$  kg (with length scale approximately  $10^{-7}$ – $10^{-6}$  m) and the spatial superposition size needing to reach approximately 10–100  $\mu\text{m}$  [14,15,21,34,48]. The larger mass objects tend to couple more strongly with their environment, such as the electromagnetic fields and collisions with residual gas particles. These couplings act as measurements, causing the collapse of the spatial superposition state into classical states, known as decoherence [49,50]. Furthermore, due to experimental constraints on the magnetic-field gradient [51,52], the time required to achieve large-scale spatial superposition states is on the order of  $\Delta t \sim 1$  s makes it more challenging to maintain the spin coherence state of NV centers and the spatial superposition state of diamond.<sup>1</sup>

For a closed-loop scheme, another challenge that is independent of the environment arises from the Humpty-Dumpty (HD) effect [55–58], which refers to the overlap problem of matter waves. For example, in the atomic interferometer mentioned above, if the wave packets on both sides

<sup>1</sup>See also gravity gradient and relative acceleration noise [33,53,54] for other sources of noise that lead to dephasing the interferometer along with electromagnetic sources of noise [18,19].

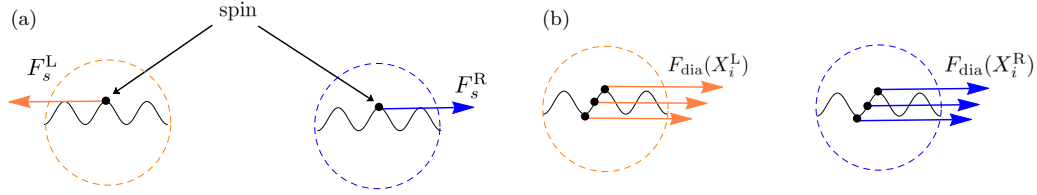


FIG. 1. Illustrations of different kinds of forces acting on the lattice chain (represented by black solid wave lines) where positions of the atom or spin are shown by black dots. The wave packets of the c.m. in the two interferometry arms denoted here by the left (L) and right (R) arms are plotted by orange and blue dashed circles. (a) Splitting forces  $F_s^{L,R}$  acting on the spin with site number  $s$  where they have the same magnitude but opposite direction. (b) Diamagnetic forces  $F_i^{L,R}$  acting on every atom, where, for simplicity, we assume it acts on the spin as well.

of the interferometer arm cannot precisely overlap (in both translational and rotational degrees of freedom), they cannot generate interference fringes and thus lead to the loss of contrast (see [59], where the analysis of the HD effect has been analyzed quite nicely, including the impact of angular momentum and the libration mode of the NV spin). For macroscopic objects, there is also a challenge of overlap due to the internal degrees of freedom, such as phonon vibration. In a very interesting work [60], the contrast reduction of phonon wave packets induced by coupling NV centers with magnetic fields was demonstrated. More recently, this coupling has been extended to white noise, providing a boundary on creating larger-scale spatial superposition states that have been considered [61].

This work also investigates the contrast loss caused by phonons in matter-wave interferometers. Unlike atomic-scale interferometers, due to the diamagnetic property of a diamond and its interaction with the magnetic field being proportional to its mass, the diamagnetic interaction becomes essential in the matter-wave interferometers with a massive object. For example, the diamagnetic interaction contributes to the trajectories of the diamond's center of mass (c.m.) wave packets. Therefore, the magnetic field must be carefully designed to guarantee a closed loop [51,62–64]. In addition, a mass-independent scheme [64] based on diamagnetic interaction creating a large superposition size has recently been proposed. From the perspective of the internal degrees of freedom, the diamagnetic repulsions of the diamonds on either side of the interferometer arms are different, leading to the excitation of varying phonon modes and thus resulting in a contrast reduction of the internal degrees of freedom. This is fundamentally similar to the spin–magnetic-field interaction in Refs. [60,61].

In this regard, our paper differs from Refs. [60,61]. We validate their results for the spin–magnetic-field interaction. However, we also consider the effect of the diamagnetic contribution, which brings another layer of complexity that is not present otherwise. In the case of the diamagnetic contribution, the phonons are also coupled to the c.m. of the diamond. The difference lies in the fact that for diamagnetic interaction, each carbon atom in the atomic chain on both sides of the interferometer arms experiences repulsion in the same direction, while for the spin–magnetic-field interaction, the chains are plucked at the NV center in opposite directions, as illustrated in Fig. 1. Besides the magnetic effects, we will also briefly mention the role of electric dipole interaction with phonons

and how it affects the latter in comparing the loss of contrast for the one-loop interferometer.

The structure of this work is arranged as follows. In Sec. II we introduce the setup, which includes the phonon model and the statistical model of phonon modes at finite temperature, and introduce the Wigner function. In Sec. III we provide the Hamiltonian of the diamond and present the model for the trajectory of the diamond wave packet. In Sec. IV we examine the different effects of diamagnetism-phonon coupling and spin-phonon interaction on phonon dynamics and further utilize displacement operators in Sec. V to describe the phonon's contrast reduction. In Sec. VI we present numerical results and compare the contrast loss induced by these two interactions at different temperatures. Also, we consider contrast loss led by other interactions, e.g., potential dipole–electric-field interaction, in the level of the phonon; this part of the discussion can be found in Appendixes D and E.

## II. BRIEF REVIEW OF PHONONS

Phonons constitute the primary focus of this work, and the model is derived from the lattice chain model (see Ref. [65]). In the case of atomic interactions, the Hamiltonian for free phonons can be expressed as

$$H_{\text{free}} = m \sum_i \frac{\dot{x}_i^2}{2} + \sum_{i,j} \frac{K_{ij}}{2} x_i x_j = \sum_q \frac{1}{2} (u_q^2 + \omega_q^2 u_q^2), \quad (1)$$

where  $K_{ij}$  is a matrix associated with the interatomic interaction while  $Q_q(X_i) = Q_q^i$  represents the eigenvector of the matrix. The position of each atom can be written as  $X_i(t) + x_i(t)$ , where the capital  $X_i(t)$  denotes the equilibrium position of the  $i$ th atom at any instant of time and  $x_i$  represents its small vibrations. Because the position of the diamond as a whole varies within the SG apparatus, the equilibrium position  $X_i(t)$  of each atom in the chain becomes a function of time. Notably, the relative distances between these equilibrium positions,  $X_{i+1} - X_i = \text{const}$ , remain constant. Therefore,  $X_i(t)$  can effectively be regarded as the trajectory of the diamond's c.m., with the distances relative to the center particle  $X_c$  remaining unchanged. Here, for convenience, we assume that the NV center (with equilibrium position  $X_s$ ) is embedded at the c.m. position  $X_c(t) = X_c$ . In the following, we sometimes neglect the time  $t$  for convenience.

The small movement  $x_i(t)$  can be expanded into mode amplitude  $u_q$ , with creation and annihilation operators as

$$x_i(t) = \frac{1}{\sqrt{Nm}} \sum_q Q_q^i u_q(t), \quad (2)$$

where the relation between  $u_q$  and its conjugate (the momentum  $\dot{u}_q$ ), and the creation and annihilation operators can be expressed as

$$\begin{aligned} a_q &= \frac{1}{\sqrt{2\hbar\omega_q}} (\omega_q u_q + i\dot{u}_q), \\ a_{-q}^\dagger &= \frac{1}{\sqrt{2\hbar\omega_q}} (\omega_q u_q - i\dot{u}_q). \end{aligned} \quad (3)$$

For simplicity, in our one-dimensional atomic chain model embedded with an NV center, we assume that all  $N$  particles have an identical atomic mass of carbon  $m$  and the mass for the diamond is  $M$ . The  $\omega_q$  is the eigenfrequency of the chain model with the fundamental tone,

$$\omega_0 = \pi c/L, \quad (4)$$

where  $c = 17.5 \times 10^3$  m/s is the sound speed within a diamond [65] and  $L$  is the length [estimated via  $L = (M/\rho)^{-1/3}$ , where the density  $\rho = 3.51 \times 10^3$  kg/m<sup>3</sup> [66]]. For example, for the masses in a range  $M \sim 10^{-14}$ – $10^{-18}$  kg the corresponding fundamental tone is in the range  $\omega_0 \sim 10^{10}$ – $10^{11}$  Hz.

At the initial stage  $t = 0$ , before the diamond enters the SG apparatus and interacts with the magnetic field, one can assume that the phonons are in a thermal equilibrium state at a temperature  $T$  [65],

$$\langle n_q(t=0) \rangle = \frac{1}{2} \coth \left( \frac{1}{2} \frac{\hbar\omega_q}{k_B T} \right). \quad (5)$$

According to the equipartition theorem, one can establish the relationship between the average number of phonons  $\langle n_q(0) \rangle$ , the characteristic length  $\sigma_{u_q}$ , and the characteristic momentum  $\sigma_{\dot{u}_q}$  as [65]

$$\langle n_q(t=0) \rangle = \frac{\omega_q}{\hbar} \sigma_{u_q}^2 = \frac{1}{\hbar\omega_q} \sigma_{\dot{u}_q}^2, \quad (6)$$

where  $\sigma_{u_q}$  and  $\sigma_{\dot{u}_q}$  are statistical averages. A review of this detail can be found in Appendix B. In the case of thermal equilibrium, the phonons in each mode  $q$  form a mixed state. The amplitudes and momenta of the phonons thus take on Gaussian distributions, represented by the Wigner function [67] as

$$W(u_q, \dot{u}_q) = \mathcal{N} \exp \left[ - \left( \frac{u_q^2}{2\sigma_{u_q}^2} + \frac{\dot{u}_q^2}{2\sigma_{\dot{u}_q}^2} \right) \right], \quad (7)$$

where  $\mathcal{N}$  is normalization factor. Equation (6) gives the normal mode's characteristic length and momentum. Note that  $\sigma_{u_q}$  and  $\sigma_{\dot{u}_q}$  are statistical averages dependent on temperature  $T$  (see Appendix B). Once we let the diamond experience the SG force, the occupation number of the phonons will evolve, and we will estimate that in the following sections.

### III. INTERACTIONS ON STERN-GERLACH APPARATUS

For the diamond embedded with a single spin  $S$  in the NV, we already assume that it has been prepared in a superposition of opposite directions  $S^R = 1$  (right) and  $S^L = -1$  (left), hence the spatial superposition. The Hamiltonian for the diamond's c.m. consists of three parts<sup>2</sup>

$$H_{\text{c.m.}} = \frac{P_c^2}{2M} - \mu S^{\text{L,R}} B - \frac{\chi_\rho M}{2\mu_0} B^2. \quad (8)$$

The first term is just the kinetic energy related to the momentum of the c.m.'s. The second term is the coupling between the NV center and the magnetic field with the magnetic moment  $\mu = g\mu_b$ , where the Landé  $g$  factor  $g \approx 2$  and Bohr magneton  $\mu_b = 9.27 \times 10^{-24}$  (J/T) [70]. For simplicity, we assume the NV is located at the c.m. with equilibrium position  $X_s = X_c$ . The appearance of the third term is because diamond is a diamagnetic material and its susceptibility is a negative value  $\chi_\rho = -6.2 \times 10^{-9}$  m<sup>3</sup>/kg [71] with vacuum permeability  $\mu_0$ . One should note that this term is a macroscopic expression. When a carbon atom chain is placed in an external magnetic field pointing in the  $\mathbf{e}_x$  direction, each carbon atom will contribute a different magnitude of repulsion according to its equilibrium position  $X_i$  pointing in the  $-\mathbf{e}_x$  direction. From the aspect of macroscopic diamond, these small repulsions collectively form a macroscopic diamagnetic force effectively acting on the c.m.,  $X_c$ .

For the magnetic field in Eq. (8), we give its form that is experienced by the  $i$ th atom as

$$B_i(t) = B_0 + b(t)X_i(t), \quad (9)$$

where  $B_0$  is the bias magnetic field and  $b(t)$  denotes the gradient in the SG apparatus. Note that in Eq. (9) the coordinates along the  $\mathbf{e}_x$  axis are represented by the uppercase  $X_i$ , indicating the equilibrium positions of atoms in the chain. For example, the magnetic field experienced by the spin, which we have assumed to be located at the center of the chain, becomes  $B_c = B_0 + b(t)X_c$ . In this model, we consider only the one-dimensional case, where the separation of the diamond and the force on the atomic chain is confined to the  $\mathbf{e}_x$  direction.

We do not consider the motion of the diamond in other dimensions, such as in drop tower experiments where the diamond needs to move in the direction of earth's acceleration or in magnetic levitation setups where it moves in a direction orthogonal to  $\mathbf{e}_x$ . In these cases, the form of a magnetic field becomes very complicated for a closed loop and it needs a careful design, especially when one takes the diamagnetic term into account [62,64]. For simplicity, we consider the movements of c.m.'s only along  $\mathbf{e}_x$ , and they are subjected only to the spin-magnetism interaction [second term in Eq. (8)]. Therefore, to get a closed loop, the magnetic

<sup>2</sup>There is also a term related to  $D(S \cdot \hat{n})^2$  related to the zero-point splitting [59,62]. This term is relevant for the internal spin degrees of freedom. Here we are not considering this contribution; we do not consider the rotation of the diamond in our current context. For the rotation of the NV center in diamond and its mechanical coupling with magnetic levitation, see [68,69].

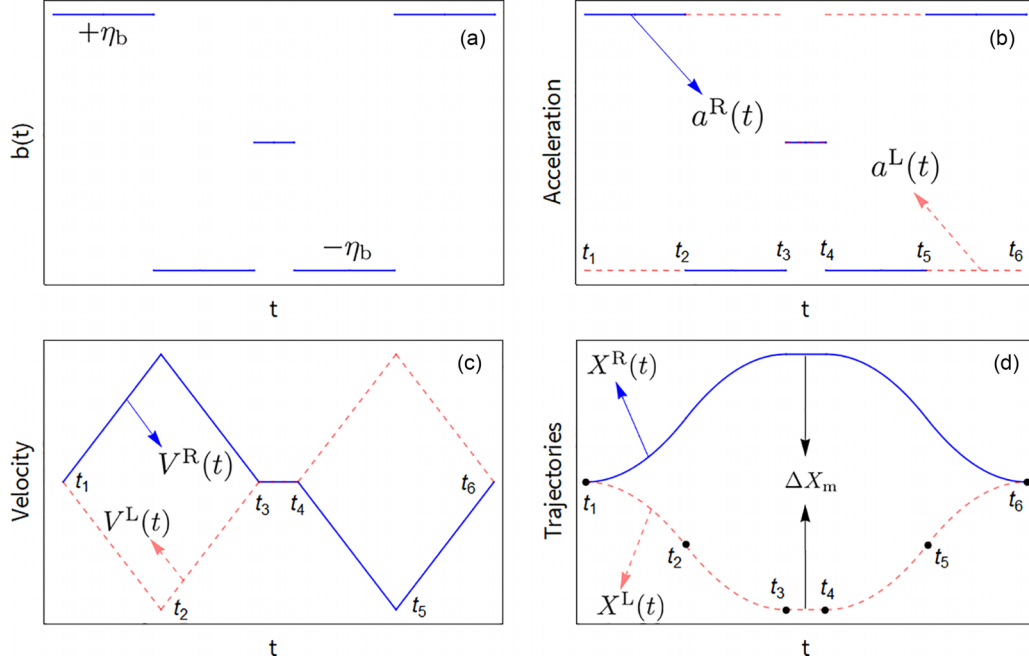


FIG. 2. (a) Magnetic-field setting inside the Stern-Gerlach apparatus and the corresponding (b) accelerations, (c) velocities, and (d) trajectories of c.m. wave packets. In the time intervals  $(t_1, t_2)$  and  $(t_5, t_6)$  the magnetic gradient is  $b(t) = +\eta_b$ , while in  $(t_2, t_3)$  and  $(t_4, t_5)$  the gradient is switched to  $b(t) = -\eta_b$ . Due to the superposition of the spin ( $S^{L,R} = \pm 1$ ), the c.m. wave packets experience opposite splitting forces due to the NV. Thus, in the left (red dashed lines) and right (blue solid lines) arms of the interferometer c.m.'s possess opposite accelerations (denoted by  $a^{L,R}$ ), velocities, and trajectories (denoted by  $X^{L,R}$ ). The duration times for acceleration and deceleration are the same as  $\tau_a$ . We also assume a free-flight process between  $t_3$  and  $t_4$  with duration  $2\tau_f$  where the magnetic gradient is turned off. Therefore, the entire time for the diamond flying inside the Stern-Gerlach apparatus is  $4\tau_a + 2\tau_f$ .

gradient  $b(t)$  can be expressed in a very simple form as [53]

$$b(t) = \begin{cases} +\eta_b, & t = [t_1, t_2] \\ -\eta_b, & t = [t_2, t_3] \\ 0, & t = [t_3, t_4] \\ -\eta_b, & t = [t_4, t_5] \\ +\eta_b, & t = [t_5, t_6], \end{cases} \quad (10)$$

where in different time intervals the gradients take constant values  $\pm\eta_b$ . The closed loop is guaranteed as long as the acceleration and deceleration durations (denoted by  $\tau_a$ ) are the same. In the interval  $[t_3, t_4]$  there is a free-flight process with duration  $\tau_f$ , where the gradient is turned off, as illustrated in Fig. 2(a).

In this paper we concentrate on the contrast loss of phonon modes, while the mismatch issue in the c.m. position and momentum of the two paths of the superposition is beyond the scope of this work. The maximum accelerations of the two paths are thus a series of constants given by

$$a^{L,R}(t) = \frac{\mu S^{L,R} b(t)}{M}. \quad (11)$$

We assume that at the initial moment, the spin inside the diamond has been prepared in a superposition and the c.m. of the diamond is at rest. When the loop starts, wave packets on either side of the interferometer behave distinctly according to  $S^R$  and  $S^L$ , with opposite accelerations as illustrated in Fig. 2(b). In this model, we neglect the acceleration due to the induced diamagnetic potential for the time being. In fact, including the effect will not modify the current scenario much,

as what matters is the relative force difference between the left and the right trajectories of the interferometer.

In this simplest case, the c.m. trajectories are symmetric, given by  $X_c^R = -X_c^L$ . As depicted in Fig. 2(d), they can be expressed by the expressions

$$X_c^{L,R}(t) = \begin{cases} \frac{a^{L,R}(t+2\tau_a+\tau_f)^2}{2}, & t = [t_1, t_2] \\ \frac{a^{L,R}(t^2-2\tau_a^2+2\tau_f t+\tau_f^2)}{2}, & t = [t_2, t_3] \\ a^{L,R}\tau_a^2, & t = [t_3, t_4] \\ \frac{a^{L,R}(t^2-2\tau_a^2-2\tau_f t+\tau_f^2)}{2}, & t = [t_4, t_5] \\ \frac{a^{L,R}(-t+2\tau_a+\tau_f)^2}{2}, & t = [t_5, t_6]. \end{cases} \quad (12)$$

Thus, the relative separation distance  $\Delta X(t)$  between the two trajectories is also a quadratic function of time. During the time interval  $[t_3, t_4]$ , this distance between the two trajectories reaches the maximum value

$$\Delta X_m = 2|a^{L,R}|\tau_a^2, \quad (13)$$

where we define the positive constant maximum acceleration  $|a^{L,R}| = \mu\eta_b/M$  and total duration time  $\Delta t = t_6 - t_1$ .

### A. Spin-phonon interaction

So far, we can observe from the Hamiltonian (8) that the diamond experiences two types of forces, i.e., the separation force acting on the NV particle located at  $X_c$  and the diamagnetic force exerted by the entire diamond, which are effectively located at the c.m. Regarding the former, the force

acts only on the central particle, the spin, which can be read out by calculating the partial derivative of the second term in Eq. (8). The splitting force has the form

$$F_s^{L,R}(t) = \mu S^{L,R} b(t), \quad (14)$$

where the index  $s$  represents the spin. From here, one can immediately write the spin–magnetic-field–phonon interaction as  $F_s x_s$  (recall that  $x_s$  represents a small vibration of the NV away from its equilibrium position). For clarity, in the following discussion related to the phonon, we refer to this coupling as the spin-phonon interaction.

### B. Diamagnetism-phonon interaction

For the diamagnetic force acting on the diamond, we consider that each particle has different magnetization opposite to the direction of the external magnetic field depending on its equilibrium position  $X_i$ . Therefore, each atom generates a different magnitude of diamagnetic repulsion  $F_{\text{dia}}^{L,R}(X_i) := F_{i,\text{dia}}^{L,R}$ . From a macroscopic perspective, the overall diamagnetic repulsion experienced by the diamond is contributed by these atoms; thus we should obtain the relationship (details of this part can be found in Appendix A)

$$F_c^{L,R} = \frac{\chi_\rho M}{\mu_0} (B_0 b + b^2 X_c^{L,R}) = \sum_i F_{i,\text{dia}}^{L,R}, \quad (15)$$

where the second part of (15) comes directly from the third term of Eq. (8), representing the overall repulsion effectively exerted on the c.m. Therefore, the coupling between the magnetic field (diamagnetism) and the  $i$ th particle (phonon) in the chain can now be written as  $F_{i,\text{dia}}^{L,R} x_i$ . In the following discussion related to the phonon, we refer to this coupling as the diamagnetism-phonon interaction.

Recalling that we used a linear magnetic field, this simple magnetic field is widely applied in interferometers [51,72]. Since the magnetic-field gradient can be modeled as a step function, the separation force (14) acting on the spin is independent of its equilibrium position  $X_s$ . Therefore, there is no coupling between the trajectories of wave packets and the phonon degrees of freedom.

In contrast to the splitting force acting on the NV center, the situation for the diamagnetic force (15) acting on each particle in the atomic chain is more complicated. The tiny vibrations of these particles (phonons) are coupled to their equilibrium positions (trajectories) through the magnetic field (considering  $F_{i,\text{dia}}^{L,R} x_i$  for each particle). Additionally, as shown in Fig. 1(a), the forces acting on the NV center in different wave packets are of the same magnitude but in opposite directions. Therefore, when the loop is completed, the contrast of phonon modes always differs by a positive or negative sign in both normal coordinates and momentum. For the diamagnetic force in Fig. 1(b), the corresponding atoms in the atomic chain of the two wave packets experience the same direction of diamagnetic force but with different magnitudes (depending on the scale of spatial superposition). It is not difficult to imagine that the phonon modes will exhibit contrast reduction under such differential influences.

### IV. PHONON FLUCTUATIONS

In this section we study a phonon excited by the two forces (14) and (15) acting on the lattice chain on the contrast of phonon wave packets. Here we generally represent the aforementioned forces as  $F_i(X_i^{L,R})$  (sometimes we will neglect  $X_i^{L,R}$  for simplicity and use just  $F_i^{L,R}$ ). The total Hamiltonian regarding every atom and their interactions with external fields can be written as

$$\begin{aligned} H_{\text{tot}} &= H_{\text{free}} - \sum_i F_i^{L,R} x_i \\ &= H_{\text{free}} - \sum_{i,q} \frac{Q_q^i F_i^{L,R}}{\sqrt{M}} u_q, \end{aligned} \quad (16)$$

where  $H_{\text{free}}$  is the free-phonon Hamiltonian in Eq. (1). Equation (16) represents the energy change of the diamond interacting with the magnetic field after entering the SG apparatus.

When the diamond enters the SG apparatus, the interaction between its internal particles and the external field changes the number of phonons. With the Hamiltonian (16), the kinematic equations for the canonical coordinates of each vibrational mode  $q$  can be derived as

$$\ddot{u}_q + \omega_q^2 u_q := f_q^{L,R} = \sum_i \frac{Q_q^i F_i^{L,R}}{\sqrt{M}}, \quad (17)$$

where  $f_q$  encompasses the forces acting on all atoms; it can be regarded as the force acting on the lattice chain. The solution of Eq. (17) is

$$\begin{aligned} u_q(t) &= u_q(0) \cos(\omega_q t) + \dot{u}_q(0) \frac{\sin(\omega_q t)}{\omega_q} \\ &\quad + \int_0^t \frac{\sin \omega_q(t-t')}{\omega_q} f_q^{L,R}(t') dt'. \end{aligned} \quad (18)$$

Here the initial conditions, i.e., the phonon amplitude  $u_q(t=0)$  and its conjugate momentum  $\dot{u}_q(t=0)$ , are solely dependent on the initial temperature of the diamond (6). The initial phonon population in mode  $q$  is (5) for the thermal equilibrium mixed state considered here. From here, it can be observed that, due to the difference in forces acting on the atomic chains on the two sides of the interference arm, a discrepancy exists in the population of phonons with mode  $q$ ,

$$n_q(t) = \frac{1}{2\hbar\omega_q} (\dot{u}_q^2 + \omega_q^2 u_q^2). \quad (19)$$

Recall that  $F_i^{L,R}$  in (17) is a generalized form introduced for convenience. When investigating spin-phonon coupling, it needs to be replaced with (14). In this case, the summation over atomic index  $i$  disappears (we consider only a single NV center). When studying the influence of the diamagnetic force of the lattice chain in different trajectories on internal degrees of freedom,  $F_i^{L,R}$  is replaced by (15) and the summation in (17) should include all atoms.

In Fig. 3 we separately illustrate the differences in the numbers of phonons induced by these two types of forces (14) and (15). Recall that the eigenvector  $Q_i^q$  of phonons is a

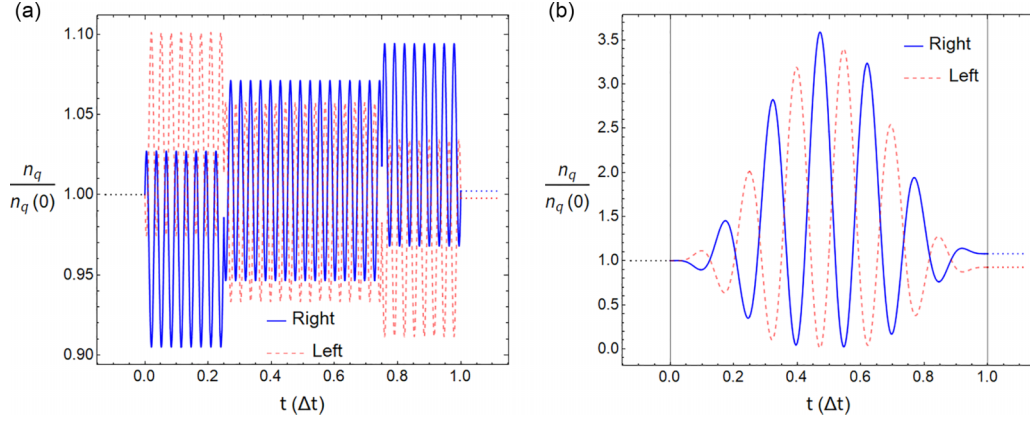


FIG. 3. Illustrations of occupation numbers of the phonons for (a) the spin-phonon interaction and (b) the diamagnetism-phonon interaction. The blue solid and red dashed curves represent the wave packets of the diamond on the right and left sides, respectively. The black dotted line represents the number of phonons in the diamond before entering the SG device (scaled to one) and the blue solid and red dotted lines represent the number of phonons on both sides after the closure of the trajectory of the diamond's c.m. Before the diamond enters the Stern-Gerlach interferometer, its wave packet is not split, so the initial number of phonons in the  $q$  mode is determined only by temperature (5). After it enters the Stern-Gerlach interferometer, the number of phonons on both sides of the interferometer arms changes over time and a difference in quantity forms. The phonon frequencies shown here [(a) 2 MHz and (b) 42 kHz] are very low, in order to achieve better visibility. For the diamond we are interested in (specifically  $10^{-14}$  kg), its natural frequency reaches  $10^{10}$  Hz. Similarly, at those frequencies, the number of phonons on both sides of the interferometer arms also forms a difference. However, since the frequency of the magnetic-field variation (especially the approximately 1 s required for the QGEM experiment) is much lower than the phonon frequencies, the change in the number of phonons in those frequency ranges is not drastic.

quantity related to the  $i$ th atom index. Here we choose it to be 1 as the upper limit. The number of phonons is constant at the initial moment. After the diamond enters the SG apparatus, the number of phonons in the two trajectories changes differently and stabilizes with a constant difference after the duration time  $\Delta t$ . Recall that we are interested in diamond masses ranging from  $M \sim 10^{-18}$  to  $10^{-14}$  kg with frequencies  $\omega_q$  in the range of  $\omega_q \sim 10^{10}$ – $10^{11}$  Hz. Therefore, the rate of change of the population of phonons of mode  $q$  is extremely rapid. Here, for visual clarity, we plot the variation in the number of low-frequency phonons in two types of interactions. One should note that, due to the size constraints of diamonds ( $\omega_0 = \pi c/L$ ), elastic waves in the material do not reach such low frequencies.

Here we introduce the difference in phonon amplitude and momentum on both sides of the interferometer arms, which arise from  $f_q^{L,R}$ ,

$$\begin{aligned} \Delta u_q &= \int_0^t \Delta f_q(t') \frac{\sin \omega_q(t-t')}{\omega_q} dt', \\ \Delta \dot{u}_q &= \int_0^t \Delta f_q(t') \cos \omega_q(t-t') dt', \end{aligned} \quad (20)$$

where we define  $\Delta f_q = f_q^R - f_q^L$ . From here, one can observe that, due to the spatial superposition of c.m.'s, the lattice chain in the two wave packets experiences different forces. In Fig. 4 we illustrate the differences in the phase space of phonon wave packets from different paths. For visual clarity, the early stage of phase evolution is faded out, and the normal coordinate and its conjugate have been made dimensionless. In [60,61] it is shown that the phase-space trajectories of phonons exhibit differences because the spin in the lattice is moving toward different directions, as shown in Fig. 4(a). In the case of diamagnetism-phonon interaction, the differences

in the force value exerted on the lattice still contribute to the reduction in contrast for phonon wave packets. In the next section we will estimate the loss of contrast due to their couplings.

## V. LOSS OF CONTRAST

The contrast in the internal degrees of freedom is defined as the inner product of the quantum states of phonons after evolving in the two interferometry arms; for a specific mode  $q$ , it becomes

$$C_q = |\langle \psi_q^L(\Delta t) | \psi_q^R(\Delta t) \rangle|. \quad (21)$$

From Eq. (21) it can be seen that the contrast is essentially the inner product of normalized phonon wave functions. Thus, a perfect closure of position, momentum, and other relevant degrees of freedom, including phonon vibrations, would yield  $C_q = 1$ , while an imperfect closure results in  $C_q \leq 1$ , indicating the loss in contrast. We employ the time-dependent perturbation theory in quantum mechanics for the time evolution of phonon quantum states. In Eq. (16) the interaction between phonons and the external field in the equation is considered as a small perturbation. Now we ignore the summation over  $q$  and focus on one mode; the Hamiltonian becomes

$$\begin{aligned} H_q &= \hbar \omega_q a_q^\dagger a_q - \sum_i F_i^{L,R} x_i \\ &= \hbar \omega_q a_q^\dagger a_q - \sum_i F_i^{L,R} Q_q^i \sqrt{\frac{\hbar}{2M\omega_q}} (a_{-q}^\dagger + a_q). \end{aligned} \quad (22)$$

Here recall that the force  $F_i^{L,R}$  is time dependent and it is subjected to the equilibrium positions  $X_i^{L,R}(t)$  of the atomic chain. Considering that the diamond is in a spatial

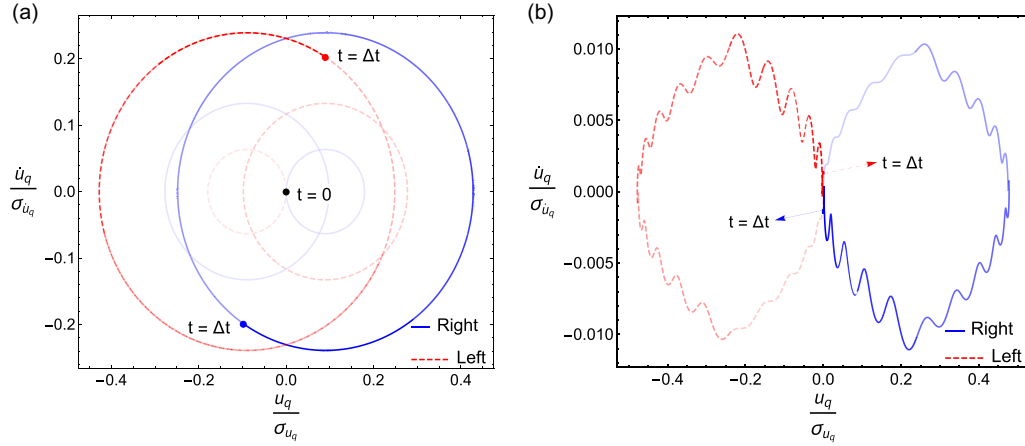


FIG. 4. Splitting in the phase space of a fixed phonon mode where the horizontal and vertical axes represent phonon amplitude and momentum, respectively. (a) Difference induced by the spin-phonon interaction. (b) Differential phase due to the diamagnetism-phonon interaction. The blue solid and red dashed curves represent the wave packets of the diamond on the right and left sides, respectively. The early stages of the phase-space trajectories are faded for clarity.

superposition state, the forces acting on the atomic chains in the two trajectories are different. In the interaction picture, denoting the time-dependent perturbation part in Eq. (22) by  $V_q(t)$ , the quantum state of the phonon obeys the Schrödinger equation. The overlap of phonon modes in the two arms becomes

$$\begin{aligned} & \langle \psi_q^L(\Delta t) | \psi_q^R(\Delta t) \rangle \\ &= \langle \psi_q(0) | \exp\left(\frac{i}{\hbar} \int_0^{\Delta t} dt' [V_q^L(t') - V_q^R(t')]\right) | \psi_q(0) \rangle \\ &= \langle \psi_q(0) | U_q^{L,\dagger} U_q^R | \psi_q(0) \rangle, \end{aligned} \quad (23)$$

where  $U_q$  is the time-evolution operator

$$U_q^{L,\dagger} U_q^R = \exp\left(\frac{i}{\hbar} (\Delta \dot{u}_q \hat{u}_q + \Delta u_q \hat{u}_q)\right). \quad (24)$$

When computing the second line of Eq. (23),  $\Delta \dot{u}_q(t)$  and  $\Delta u_q(t)$  emerge, which are precisely defined in Eq. (20). In Eq. (24) one can first consider the case of spin-phonon coupling (14). In this case,  $V_q^L$  and  $V_q^R$  differ exactly by a positive or negative sign, which is because the forces exerted on the phonon wave packets on both sides of the interferometer arms happen to be in opposite directions. In this scenario, the amplitudes and momentum of the phonons on both sides of the interferometer arms are displaced in opposite directions by  $\frac{1}{2} \Delta u_q$  and  $\frac{1}{2} \Delta \dot{u}_q$ , respectively. The contrast of the phonon can be comprehended as the probability of its amplitude and momentum staying in the initial state  $\psi_q(0)$  [60] as shown in Fig. 4(a); once the two wave packets are separated, the overlap would not be perfect.

For the diamagnetism-phonon interaction, the decrease in contrast is also not difficult to imagine. In this case, the amplitudes and corresponding momentum of the phonons on both sides of the interferometer arms are displaced to varying degrees in the same direction. One can always utilize Eq. (23) to calculate the contrast of the phonon wave function (details

are given in Appendix C) as

$$\begin{aligned} C &= |\langle \psi_q^L(\Delta t) | \psi_q^R(\Delta t) \rangle| \\ &= \prod_q |\text{Tr}[U_q^{L,\dagger} U_q^R | \psi_q(0) \rangle \langle \psi_q(0) |]| \\ &= \prod_q |\text{Tr}[U_q^{L,\dagger} U_q^R \rho_q(0)]|. \end{aligned} \quad (25)$$

Here we have considered an initial thermal equilibrium ensemble of phonons composed of a state  $\rho_q(0)$ .

Note that to evaluate the contrast (25), it is equivalent to evaluate the mean value of  $U_q^{L,\dagger} U_q^R$ , which consists of both the phonon's ‘‘position’’ and its conjugate. Therefore, it is convenient to calculate the mean value by using the Wigner function, which is a quasidistribution of the phonon's position and momentum in phase space, where, for the harmonic mode considered here, it has a form of the double Gaussian (7).

Therefore, in the end, by multiplying the exponential operator with Eq. (7) and integrating over  $u_q$  and  $\dot{u}_q$ , the contrast becomes

$$\begin{aligned} C_q &= \text{Tr}[U_q^{L,\dagger} U_q^R \rho_q(0)] \\ &= \exp\left(-\frac{\coth \frac{1}{2} \frac{\hbar \omega_q}{k_B T}}{4 \hbar \omega_q} \left| \int_0^{\Delta t} \Delta f_q(t) e^{i \omega_q t} dt \right|^2\right) \\ &= \exp\left(-\frac{\coth \frac{1}{2} \frac{\hbar \omega_q}{k_B T}}{4 \hbar \omega_q} |\Delta \tilde{f}_q(\omega_q)|^2\right). \end{aligned} \quad (26)$$

The final result of the contrast is an exponential function and is temperature dependent. Naturally, when  $\Delta \tilde{f}_q(\omega_q)$  is zero, interference arms on both sides will exhibit no distinction and Eq. (26) will yield a result of 1. However, if there is a difference in the forces acting on the lattice chain on both sides of the interference arms, then  $C \neq 1$  and the loss of

contrast<sup>3</sup> is expressed as  $\ln C$ . The Fourier transform

$$\Delta \tilde{f}_q := \Delta \tilde{f}_q(\omega_q) = \left| \int_0^{\Delta t} \Delta f_q(t) e^{i\omega_q t} dt \right| \quad (27)$$

represents a power spectrum that is a function of  $\omega_q$  and  $\Delta t$ , determining the value and properties of the contrast. In the study of noise in SG devices, macroscopic noise is transformed into the phase fluctuation through this transform. Thus it is also referred to as the transfer function [33] (see also [53]). The transfer function is closely related to the trajectory of the interference arms. For the simplest acceleration protocol (Fig. 1), the transfer function of the splitting force is very trivial, transforming two constant accelerations. The resulting  $f_q(\omega_q)$  for this transformation only contains  $1/\omega_q$ . However, for forces closely related to the trajectory, their transfer function contains powers of  $(1/\omega_q)^n$ . In the following sections, we will compute the contrast.

## VI. NUMERICAL RESULTS

In this section we numerically explore contrast reduction due to phonon wave packets from the interactions given in Eq. (8). Since we do not want the magnetic-field gradient, which controls the spatial superposition size, to be too large, i.e.,  $\eta_b \leq 10^6$  T/m (see [46,73], where such gradients could be achieved), the maximum spatial separation distances  $\Delta X_m \sim 10^{-6}$ – $10^{-3}$  m for different masses. For simplicity, here we consider phonons as longitudinal elastic waves,  $\omega_q = cq$  [67], and treat them as continuous with a minimum frequency (fundamental frequency)  $\omega_0 = \pi c/L$ . In addition, we take the eigenvector  $Q_q^i = 1$  (recall that in solid-state physics, these vectors are sinusoidal functions) as an upper limit. We also define the moment when the diamond wave packet reaches its maximum separation distance  $\Delta X_m$  at time  $t = 0$ . Thus,  $t_1 = -2\tau_a - \tau_f$  and  $t_6 = -t_1 = 2\tau_a + \tau_f$ .

To compute Eq. (26), we need to convert Eqs. (14) and (15) into respective transfer functions. Here we first provide their forms in the temporal domain as differences on both sides of the interferometer arms,

$$\begin{aligned} \Delta F_s(t) &= \mu(S^R - S^L)\eta_b = 2\mu\eta_b, \\ \Delta F_{\text{dia}}(t) &= \sum_i (F_{i,\text{dia}}^R - F_{i,\text{dia}}^L) \\ &= \frac{\chi_\rho M}{\mu_0} \eta_b^2 (X_c^R - X_c^L). \end{aligned} \quad (28)$$

The differential force for spin-phonon interaction is easily understood in (28). These are the constant differences between the left and right interferometer arms at different time stages.

<sup>3</sup>From the expression of contrast, one can directly see why high temperature will destroy contrast. Suppose  $T \rightarrow \infty$  for a fixed  $\omega_q$ . Then the expression for the exponential part of Eq. (26) is  $-\frac{k_B T}{2\hbar^2 \omega_q^2} |\Delta \tilde{f}_q|^2 \rightarrow -\infty$ . Therefore,  $C \rightarrow 0$ . The transfer function  $\Delta \tilde{f}_q$  is always nonzero in our case. In the other limit, when  $\omega_q \sim cq \rightarrow 0$ , for a finite temperature, again  $C \rightarrow 0$ . Lower values of  $\omega_q$  can occur for systems with a lower speed of sound. Typically, these are more compressible objects for which the speed of sound is lower than that of the diamondlike system.

Recall that  $\eta_b$  is the maximum value of the magnetic-field gradient.

Likewise, for the diamagnetism-phonon coupling, due to the diamond wave packet being in a spatial superposition, there is also a difference of the diamagnetic repulsion generated by the atoms located on the two sides of the interferometer arms (for example, the  $i$ th atom with positions  $X_i^{\text{L,R}}$ ). Thereafter, we can obtain their corresponding transfer functions

$$\begin{aligned} |\Delta \tilde{f}_s(\omega_q)|^2 &= M \left( \frac{2\Delta X_m}{\tau_a^2 \omega_q} \right)^2 \Gamma^2(\omega_q), \\ |\Delta \tilde{f}_{\text{dia}}(\omega_q)|^2 &= M^5 \left( \frac{\chi_\rho \Delta X_m^3}{2\mu_0 \mu^2 \tau_a^6 \omega_q^3} \right)^2 \Gamma^2(\omega_q). \end{aligned} \quad (29)$$

In Sec. III the coupling of the magnetic field with the spin generates the spatial superposition state of the diamond wave packet. Here we parametrize the trajectory, acceleration, magnetic-field gradient, and other parameters of the wave packet in terms of the acceleration duration  $\tau_a$ , mass  $M$ , and maximum separation distance  $\Delta X_m$ . The  $\Gamma(\omega_q)$  here arises from the Fourier transform. For the two types of interactions, their forms are the same,

$$\Gamma(\omega_q) = \sin[(\tau_f)\omega_q] - 2 \sin[(\tau_a + \tau_f)\omega_q] + \sin[(2\tau_a + \tau_f)\omega_q]. \quad (30)$$

Substituting the corresponding transfer function in Eq. (29) into Eq. (26), we can obtain the expression for the contrast reduction brought about by these interactions,

$$\begin{aligned} -\ln C_{\text{spin}} &= \sum_q \coth \left( \frac{1}{2} \frac{\hbar \omega_q}{k_B T} \right) \frac{M \Delta X_m^2}{\tau_a^4 \omega_q^3 \hbar} \Gamma^2(\omega_q), \\ -\ln C_{\text{dia}} &= \sum_q \coth \left( \frac{1}{2} \frac{\hbar \omega_q}{k_B T} \right) \frac{\chi_\rho^2}{16\mu_0^2 \mu^4 \hbar} \frac{M^5 \Delta X_m^6}{\tau_a^{12} \omega_q^7} \Gamma^2(\omega_q). \end{aligned} \quad (31)$$

Note that since we start from a one-dimensional atomic chain model, the mass  $M$  in (31) and (32) should in principle be understood as the mass of a single atomic chain within the diamond. However, in the subsequent calculations, we will interpret this  $M$  as the total mass of an isotropic homogeneous cubic diamond with side length  $L = (M/\rho)^{1/3}$ , where the main contribution to contrast loss comes from the fundamental tone  $\omega_0 = \pi c/L$ .<sup>4</sup>

In Fig. 5 we show the contrast reduction resulting from spin-phonon (solid lines) and diamagnetism-phonon (dashed and dotted lines) interactions in a setup with  $\Delta t = 1$  s. The horizontal axis represents the maximum separation distance of the diamond's c.m.'s in the spatial superposition state. The black ( $10^{-14}$  kg) and red ( $10^{-18}$  kg) lines compare diamonds of different masses. We also compared the contrast loss at

<sup>4</sup>Phonon modes depend on the shape of three-dimensional objects. Studies on acoustic phonons in circular objects can be found in [74]. The situation becomes considerably more complex for arbitrary-shaped three-dimensional objects and deserves separate discussion.



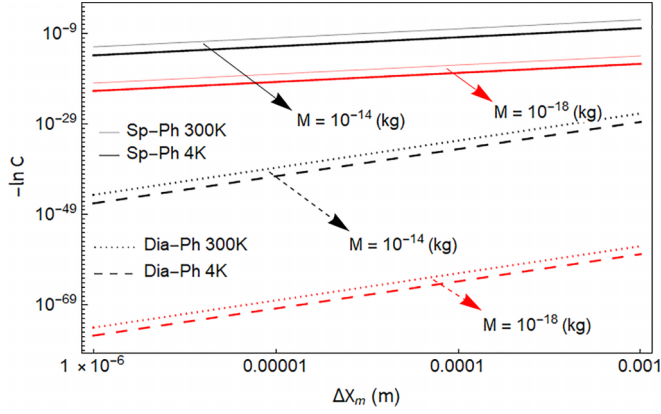


FIG. 5. Phonon-induced contrast loss caused by spin-phonon (Sp-Ph, solid lines) and diamagnetism-phonon (Dia-Ph, dashed and dotted lines) interactions in the expected scenario of the QGEM experiment (with a duration time of approximately 1 s). The horizontal axis  $\Delta X_m$  is the maximum separation distance between diamond wave packets on either side of the interferometer. From Eqs. (31) and (32), the contrast loss caused by phonon modes will be zero when  $\Delta X_m = 0$ , indicating no spatial separation. The contrast loss from heavier mass  $M = 10^{-14}$  kg (four black lines) is correspondingly greater than that for the smaller mass  $M = 10^{-18}$  kg (four red lines). Also depicted are scenarios at different temperatures, showing that the phonon-induced contrast loss at 300 K is greater than that at 4 K.

different temperatures,<sup>5</sup> where the results at low temperature (4 K) are presented by dark solid and dashed lines, while at high temperature (300 K) results are shown by light solid and dotted lines. The results indicate that the contrast loss induced by the spin-phonon coupling is dominant, while the effect of diamagnetism-phonon interaction is significantly smaller.

<sup>5</sup>The main contribution of contrast loss comes from the fundamental frequency  $\omega_0 \sim c/L$ . One can consider two limits here, one is  $\hbar\omega_0 \ll k_B T$  and the other is  $\hbar\omega_0 \gg k_B T$ . For the former limit, the square of the transfer function will yield the maximum value of  $|\Gamma(\omega_0)|^2 \sim 1$ , and Eqs. (31) and (32) become

$$-\ln C_{\text{spin}} \approx \frac{2k_B T}{\hbar^2} \frac{M \Delta X_m^2}{\tau_a^4 \omega_0^4} \sim \frac{2k_B T}{\hbar^2} \rho \left( \frac{\Delta X_m}{c^2 \tau_a^2} \right)^2 L^7,$$

$$-\ln C_{\text{dia}} \approx \frac{k_B T \chi_\rho^2}{8\hbar^2 \mu_0^2 \mu^4} \frac{M^5 \Delta X_m^6}{\tau_a^{12} \omega_0^8} \sim \frac{k_B T \chi_\rho^2 \rho^5}{8\mu_0^2 \mu^4 \hbar^2} \left( \frac{\Delta X_m}{c^4 \tau_a^6} \right)^2 L^{23},$$

respectively. In the other limit, when  $\hbar\omega_0 \gg k_B T$  the hyperbolic function  $\coth \frac{1}{2} \frac{\hbar\omega_0}{k_B T} \rightarrow 1$ . The contrast reductions from the two interactions become

$$-\ln C_{\text{spin}} \approx \frac{M \Delta X_m^2}{\hbar \tau_a^4 \omega_0^3} \sim \frac{\rho}{\hbar c^3} \left( \frac{\Delta X_m L^3}{\tau_a^2} \right)^2,$$

$$-\ln C_{\text{dia}} \approx \frac{\chi_\rho^2}{16\mu_0^2 \mu^4 \hbar} \frac{M^5 \Delta X_m^6}{\tau_a^{12} \omega_0^7} \sim \frac{\chi_\rho^2 \rho^5}{16\mu_0^2 \mu^4 \hbar c^7} \left( \frac{\Delta X_m L^{11}}{\tau_a^6} \right)^2.$$

In the above two limits, we used the relation  $M = \rho L^3$ , where  $\rho$  is the density of test masses and  $L$  is the length. In either of the limits, one can always conclude that more rigid material (which means faster sound speed) and smaller size of the test masses will produce less reduction in contrast. The diamondlike crystal would be an example of an ideal crystal for the QGEM experiment.

The source of these differences can be easily understood by comparisons in Eqs. (31) and (32). The contrast reduction caused by the former interaction is suppressed by  $\omega_q^3$ , whereas the contrast loss caused by diamagnetism-phonon interaction is suppressed by  $\omega_q^7$ .

Moreover, room temperature does not drastically alter the outcomes for either of them. Additionally, it can be observed that larger diamond masses lead to more phonon contrast reduction, which is quite understandable. Larger mass implies a lower range of phonon frequencies. From Eqs. (26) and (29) it can be seen that these  $\omega_q$  terms appear in the denominators.

From Eq. (26) we can see that the acceleration protocol profoundly impacts the contrast of the phonon wave packets. In Fig. 6 we use a density plot to detail the contrast reduction resulting from different acceleration protocols. In each plot we highlight the black curves, where the magnetic-field gradient is precisely  $10^6$  T/m, and in the region above it, the duration time is longer, thus requiring a smaller magnetic-field gradient. In Figs. 6(a) and 6(b) we study the contrast of a diamond with a mass of  $M = 2.25 \times 10^{-14}$  kg for different maximum separation distances  $\Delta X_m$  and duration times. In Figs. 6(c) and 6(d) we set the maximum separation distance of the c.m.'s to  $10^{-4}$  m, which represents a sufficiently large separation distance of wave packets in QGEM, and study the contrast loss for different diamond masses and duration times.

From Figs. 6(a) and 6(b) one can see that for  $10^{-14}$  kg diamond, when the separation protocol requires the loop to be completed within a short time (for example, 0.05 s) while reaching large separation distance  $\Delta X_m$ , the loss of contrast from both interactions could go to 1%. Likewise, in Figs. 6(c) and 6(d), for large spatial separation as expected by the QGEM (for example,  $10^{-4}$  m), protocols with heavier diamond and shorter duration time  $\Delta t$  would also lead to severe contrast reduction in phonon degrees of freedom. Overall, significant contrast loss will happen when wave packets of a large mass diamond are separated over a large spatial distance within a short period. However, within the current experimental constraints where the SG magnetic field is constrained to be less than  $10^6$  T/m [46,73], the contrast loss induced by both couplings is negligible for QGEM.

## VII. DISCUSSION

In this paper we have analyzed the contrast loss due to phonons in creating a spatial superposition of a nanoscaled diamond embedded with a single NV center based on a Stern-Gerlach interferometer. During the process of creating a spatial superposition state using the coupling between the spin and the linear magnetic field, the spin particle in the lattice chain generates a pair of forces (14) of opposite directions and equal magnitudes due to their own spin superposition state. Similar to the Humpty-Dumpty problem at the center of mass of the diamond, the spin particles on both sides of the interferometer arm have different vibrational states in the lattice, resulting in differences in the quantum states of the phonons. This also leads to imperfections in the overlap of phonon wave packets.

The other interaction arises from the diamagnetic properties of diamond. Each atom in the lattice chain produces

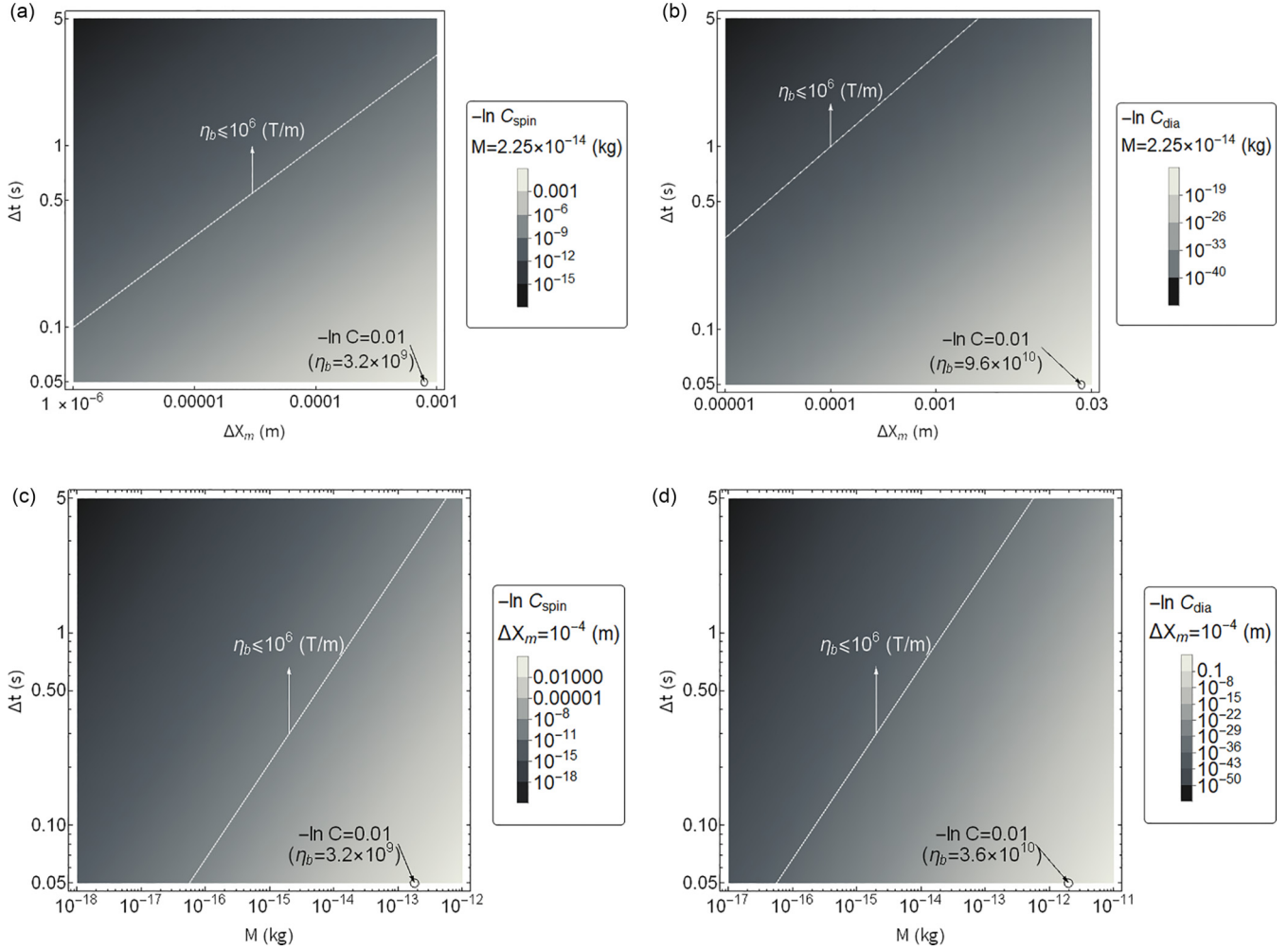


FIG. 6. Contrast reduction resulting from (a) and (c) spin-phonon coupling and (b) and (d) diamagnetism-phonon interaction under different close-loop protocols, where the color shading from dark to light represents progressively intensified contrast reduction. (a) and (b) Scenarios with a diamond mass of  $M \sim 2.25 \times 10^{-14}$  kg, showing different maximum separations  $\Delta X_m$  (horizontal axis) and duration times  $\Delta t$  (vertical axis). (c) and (d) A desired separation distance of  $\Delta X_m = 10^{-4}$  m is assumed for the diamond's c.m.'s. We explore the contrast loss caused by phonon wave packets of different masses under varying duration times. We have marked the cases where the contrast loss reaches 1%. For a diamond with mass  $M = 2.25 \times 10^{-14}$  kg, significant contrast loss requires achieving maximum separation distances of (a) approximately  $10^{-3}$  m and (b) approximately  $10^{-2}$  m for the c.m. wave packet within 0.05 s. To achieve  $\Delta X_m = 10^{-4}$  m within 0.05 s, the diamond mass needs to reach (c) approximately  $10^{-13}$  kg and (d)  $10^{-12}$  kg to exhibit significant contrast loss. In these four cases marked, the magnetic gradients required are all large, becoming approximately 1000–10 000 times greater than the current experimental capability.

a diamagnetic force (15) when subjected to an external magnetic field. This diamagnetic force is of the same direction but has a different magnitude on both sides of the interferometer arm. Similarly, due to this difference, the quantum states of phonons on both sides are also different, resulting in contrast reduction.

In this paper we used a linear magnetic field (9), which is widely used in atomic interferometers. Furthermore, this linearity greatly simplifies the calculation of the motion state of spin particles, that is, the splitting force is independent of trajectories and the equilibrium position.

The situation is more complex regarding the interaction between the diamagnetic force and phonons. Since the diamagnetic term in the Hamiltonian includes  $B(X_i)^2$ , the force on the lattice is now coupled with its trajectory. This external-field-mediated coupling between the phonon and

c.m. trajectory is common in the study of optical cooling of the motion state of diamond center. In this work we typically studied the latter situation and compared the contrast reduction between these two interactions.

Specifically, we assumed that the phonons were initially at a specific temperature  $T$  and we utilized the Wigner representation to express and compute the evolution of the quantum state of the phonons. Our results indicate that of these two sources contributing to the contrast loss in the phonon degrees of freedom, the effect of the spin-phonon coupling is dominant. The contrast loss induced by the diamagnetic term is smaller than the former, as shown in Fig. 5. This result can be directly understood from (31) and (32). For the spin-phonon coupling, which does not depend on the trajectory, the contrast reduction is suppressed by the phonon frequency to the power of 3. Meanwhile, the contrast loss due to

diamagnetism-phonon interaction is suppressed by the phonon frequency to the power of 7.

The latter case directly arises from its coupling with the trajectory, as the diamagnetic force is a function of time and its variation is adiabatic. In the seminal work in [60,61], this is also referred to as the degree of adiabaticity.

However, overall, the contrast reduction induced by both interactions is minimal. This is good news for matter-wave interferometers. There are two main reasons for this result. One is that we limit the gradient of the magnetic field. The most important reason, however, is that we are studying diamonds of very small size ( $10^{-20}$ – $10^{-14}$  kg) compared to the speed of sound  $c$  multiplied by the duration time (on the order of microseconds and 1 s for QGEM). Since the frequencies of the phonons are very high (tens of gigahertz to several terahertz), their contribution to contrast loss is tiny. However, if we prefer a different material where the speed of sound is much lower than that of the diamond, we would see the loss of contrast occur. However, it also depends on how we create the superposition; hence, it depends on the details of the transfer function.

#### ACKNOWLEDGMENT

S.B. is grateful for support through EPSRC Grants No. EP/R029075/1, No. EP/X009467/1, and No. ST/W006227/1. Q.X. and R.Z. were supported by the China Scholarship Council.

#### APPENDIX A: DIAMAGNETIC REPULSION

From Eq. (8) one can immediately write the diamagnetic repulsion given by the entire diamond,

$$F_{\text{dia}}^{\text{L,R}} = \partial_X \frac{\chi_\rho M}{2\mu_0} B^2(X)|_{X=X_c^{\text{L,R}}} = \frac{\chi_\rho M}{\mu_0} (B_0 \eta_b + \eta_b^2 X_c^{\text{L,R}}). \quad (\text{A1})$$

The diamagnetic force here is a macroscopic quantity, representing the repulsion of the entire diamond to the magnetic field, which is effectively located at the c.m. with equilibrium position  $X_c$ . However, unlike the splitting force which acts on the central particle, this does not mean that the repulsion exhibited by particles in the middle of the atomic chain is equal to Eq. (A1).

Here we consider that each atom in the atomic chain is magnetized with the potential energy  $U(X_i)$ . We will not delve into the specific form of this  $U(X_i)$ , but in general it is the product of the magnetization of a single carbon atom and the magnetic-field strength experienced by that atom (relevant discussion can be found in Chap. 4 of [75]). Therefore, each atom will contribute a different diamagnetic force, and these microscopic diamagnetic forces will vary in magnitude due to the different equilibrium positions of the atoms,

$$F_{i,\text{dia}}^{\text{L,R}} = -\partial_X U(X)|_{X=X_i^{\text{L,R}}}. \quad (\text{A2})$$

The summation over the index  $i$  of these microscopic diamagnetic forces must be equal to Eq. (A1), and thus we have the relation (15).

#### APPENDIX B: INITIAL THERMAL EQUILIBRIUM MIXED STATE

Here we provide supplementary information about characteristic length and characteristic velocity for phonons in (6). Consider that, before any interaction between fields, the quantum oscillator system for mode  $q$  is

$$H_{\text{free}} = \frac{1}{2}(\dot{u}_q^2 + \omega_q^2 u_q^2). \quad (\text{B1})$$

The eigenenergy of this simple Hamiltonian is obviously  $E_n = \hbar\omega_q(n + \frac{1}{2})$ , where  $n$  is the phonon number in mode  $q$ . In this pure state, there is no ensemble to work with. Now let us consider that, initially, there are various phonon modes in the diamond where they have reached a thermal equilibrium state with the partition function,

$$\begin{aligned} Z &= \sum_n e^{-\beta E_n} \\ &= e^{-(\beta/2)\hbar\omega_q} \sum_{n=0}^{\infty} e^{-n\beta\hbar\omega_q} \\ &= \frac{1}{2 \sinh\left(\frac{\beta}{2}\hbar\omega_q\right)}, \end{aligned} \quad (\text{B2})$$

where  $\beta = 1/k_B T$ . The calculation from the second to the third line in Eq. (B2) can be found in, for example [75]. The average energy is thus

$$\langle E \rangle_q = -\frac{\partial \ln Z}{\partial \beta} = \frac{\hbar\omega_q}{2} \coth\left(\frac{\beta}{2}\hbar\omega_q\right). \quad (\text{B3})$$

Note that the equipartition theorem tells us that the collections of the phonon's potential energies and kinetic energies are the same such that we have

$$\left\langle \frac{\dot{u}_q^2}{2} \right\rangle = \left\langle \frac{\omega_q^2 u_q^2}{2} \right\rangle = \frac{\langle E \rangle_q}{2} = \frac{\hbar\omega_q}{4} \coth\left(\frac{\beta}{2}\hbar\omega_q\right). \quad (\text{B4})$$

Therefore, the square of the characteristic width and velocity becomes

$$\begin{aligned} \sigma_{u_q}^2 &= \langle \dot{u}_q^2 \rangle = \frac{\hbar\omega_q}{2} \coth\left(\frac{\beta}{2}\hbar\omega_q\right), \\ \sigma_{u_q}^2 &= \langle u_q^2 \rangle = \sigma_{u_q}^2 = \frac{\hbar}{2\omega_q} \coth\left(\frac{\beta}{2}\hbar\omega_q\right). \end{aligned} \quad (\text{B5})$$

#### APPENDIX C: OVERLAP AND WIGNER REPRESENTATION

Here we provide some details about Eq. (23). We can represent the time evolution of the phonon wave function in the interaction picture for a specific mode  $q$  as

$$|\psi_{I,q}^{\text{L,R}}(t)\rangle = \exp\left(-\frac{i}{\hbar} \int_0^t dt' V_q^{\text{L,R}}(t')\right) |\psi_q^{\text{L,R}}(0)\rangle. \quad (\text{C1})$$

We have set  $|\psi_{I,q}(0)\rangle = |\psi_q(0)\rangle$ , where  $|\psi_q(0)\rangle$  is a stationary state in the Schrödinger picture. We have also ignored a global phase factor that does not contribute to the contrast. One can express the interaction potential in terms of the phonon mode

amplitude and momentum as

$$\begin{aligned} V_q^{\text{L,R}}(t) &= -\sum_i F_i^{\text{L,R}} Q_q^i \sqrt{\frac{\hbar}{2M\omega_q}} (\hat{a}_{-q}^\dagger e^{i\omega_q t} + \hat{a}_q e^{-i\omega_q t}) \\ &= -\sum_i \left( \hat{u}_q \frac{F_i^{\text{L,R}}}{\sqrt{M}} Q_q^i \cos(\omega_q t) + \hat{u}_q \frac{F_i^{\text{L,R}}}{\sqrt{M}} Q_q^i \frac{\sin(\omega_q t)}{\omega_q} \right) \\ &= -\hat{u}_q \cos(\omega_q t) f_q^{\text{L,R}} - \hat{u}_q \frac{\sin(\omega_q t)}{\omega_q} f_q^{\text{L,R}}. \end{aligned} \quad (\text{C2})$$

The  $f_q^{\text{L,R}}$  has already been defined in Eq. (17) and the relation between the creation and annihilation operators and phonon amplitude can be found in (2) and (3). The overlap of the wave functions of phonons on both sides of the interferometer arm can be expressed as

$$\begin{aligned} &\langle \psi^{\text{L}}(\Delta t) | \psi^{\text{R}}(\Delta t) \rangle \\ &= \langle \psi_1(0) | \exp\left(\frac{i}{\hbar} \int_0^{\Delta t} dt' [V_q^{\text{L}}(t') - V_q^{\text{R}}(t')]\right) | \psi_1(0) \rangle \\ &= \langle \psi_1(0) | \exp\left[\frac{i}{\hbar} \int_0^{\Delta t} dt' \left( \hat{u}_q \cos(\omega_q t) \Delta f_q \right. \right. \\ &\quad \left. \left. + \hat{u}_q \frac{\sin(\omega_q t)}{\omega_q} \Delta f_q \right)\right] | \psi_1(0) \rangle. \end{aligned} \quad (\text{C3})$$

The integral terms in the third line of Eq. (23) precisely represent the differences in phonon amplitudes and momentum given in Eq. (20). Here one can observe that if the force acting on the atomic chain is coupled with the spin and magnetic field, then  $V_1^{\text{L}} = -V_1^{\text{R}}$ . For diamagnetic interaction, since the diamagnetic force points in the same direction, the situation is different.

We use the Wigner representation to calculate the average of (23). In the Wigner representation, the average of an operator  $\hat{A}(x)$  can be calculated as

$$\langle \hat{A} \rangle = \iint W(x, p) \tilde{A}(x, p) dx dp, \quad (\text{C4})$$

where  $W(x, p)$  is the Wigner function, which provides a quasidistribution of the quantum state simultaneously in position  $x$  and momentum  $p$  space. Usually, in the Wigner representation, one typically needs to utilize the Weyl transform to express the operator  $\hat{A}$  as a function  $\tilde{A}(x, p)$ . In this context, the exponential operator in (C3) is already a function of phonon normal coordinates and their conjugates. We first consider a pure state of phonons in mode  $q$ . Its ground-state wave function can be expressed as

$$\psi(u_q) = \left(\frac{\omega_q}{\pi \hbar}\right)^{1/4} e^{-\omega_q u_q^2 / 2\hbar}. \quad (\text{C5})$$

The Wigner function is defined as

$$\begin{aligned} W(u_q, \dot{u}_q) &= \frac{1}{2\pi \hbar} \int_{-\infty}^{\infty} e^{i\dot{u}_q y} \psi\left(u_q + \frac{y}{2}\right) \psi^*\left(u_q - \frac{y}{2}\right) dy \\ &= \frac{1}{\pi \hbar} \exp\left[-\left(\frac{u_q^2}{2\left(\frac{\hbar}{2\omega_q}\right)} + \frac{\dot{u}_q^2}{2\left(\frac{\hbar\omega_q}{2}\right)}\right)\right], \end{aligned} \quad (\text{C6})$$

where  $\frac{\hbar}{2\omega_q}$  and  $\frac{\hbar\omega_q}{2}$  relate to the characteristic width and velocity, respectively. In the thermal equilibrium mixed state, one needs to replace

$$\frac{\hbar\omega_q}{2} \rightarrow \frac{\hbar\omega_q}{2} \coth \frac{\hbar\omega_q}{2k_B T}, \quad \frac{\hbar}{2\omega_q} \rightarrow \frac{\hbar}{2\omega_q} \coth \frac{\hbar\omega_q}{2k_B T}. \quad (\text{C7})$$

#### APPENDIX D: CONTRAST LOSS DUE TO INTRINSIC DIPOLE-PHONON COUPLING

In this Appendix we present the contrast loss due to dipole-phonon coupling. It is worth noting that the dipole-phonon coupling we consider does not involve energy-level transitions of the dipole, such as in the Jaynes-Cummings model. We consider only the overlap of the positions and momenta of the phonons on both sides of the interferometer arm, that is, the motion state of the phonons.

Here let us first consider the case of an intrinsic dipole. In diamond materials embedded with NV centers, due to the NV center itself carrying a negative charge, the inevitable occurrence of compensatory positive charges arises when it replaces a carbon atom in the material. As a result, a dipole moment  $d_0$  arises, and its specific value depends on the distance from the compensatory positive charges to the NV center. This value is approximately 1 D. Here we aim to study the effect of the dipole on lattice vibrations through its interaction with an external electric field. Therefore, we assume that this intrinsic dipole overlaps with the NV center, meaning that the compensatory positive charges and the NV center are located in the same lattice site.

As in the analysis in the main text, let us denote the position of a single intrinsic dipole by  $X_c(t) + x_c$ , where  $X_c(t)$  represents the equilibrium position, while  $x_c$  represent the dipole's vibration. The dipole-phonon interaction Hamiltonian is again mediated by an extra electric field  $E(X_c)$  as

$$H_{\text{intrinsic}} = -d_0 E(X_c). \quad (\text{D1})$$

Recall that the diamond has its trajectories as illustrated in Fig. 2. The  $X_c$  can be expressed explicitly as (12) and  $E(X_c)$  represents the electric field experienced by the dipole.

Again, due to the dipole being in a spatial superposition state (considering the diamond entering the SG apparatus), if there is a difference in the derivatives of  $E(X_c)$  on both sides of the interferometer arm, there will be differences in the amplitudes and momentum of the phonons, as illustrated in (20). Obviously, if  $E(X_c)$  is linear, the coupling between the dipole and the electric field will not cause such differences.

#### APPENDIX E: CONTRAST LOSS DUE TO INDUCED DIPOLE-PHONON COUPLING

This Appendix presents an analysis of the induced dipole-phonon coupling on phonon contrast loss. Similarly, we consider only the motion state of the phonons and do not consider the energy-level issues of the dipole. We consider that each  $i$ th particle in the atomic chain experiences an external linear electric field

$$E(X_i) = E_0 + \eta_c X_i(t), \quad (\text{E1})$$

where the constant electric gradient is labeled  $\eta_e$ . Again, particles move parallel to the diamond's trajectories, and their equilibrium positions  $X_i$  become functions of time. Due to the fact that the diamond is a dielectric material when subjected to the external electric field, an induced dipole will be generated in each atom of the lattice chain as

$$d_i(X_i) = \frac{\alpha}{\epsilon_r} E(X_i), \quad (\text{E2})$$

where  $\epsilon_r \approx 5.7$  is the relative dielectric constant and the polarizability  $\alpha$  is given by the Clausius-Mossotti relation

$$\frac{\alpha N}{3\epsilon_0 V} = \frac{\epsilon_r - 1}{\epsilon_r + 2}, \quad (\text{E3})$$

where  $V$  is the volume of the diamond. Therefore, the interaction Hamiltonian with the external electric field can be expressed as

$$\begin{aligned} H_{\text{induced}} &= - \sum_i d_i(X_i) E(X_i) \\ &= - \sum_i \frac{\alpha}{\epsilon_r} E^2(X_i). \end{aligned} \quad (\text{E4})$$

The force exerted on the  $i$ th particle can be written straightforwardly as

$$F_i^{\text{dp}} = \frac{2\alpha}{\epsilon_r} E_0 \eta_e + \frac{2\alpha}{\epsilon_r} \eta_e^2 X_i. \quad (\text{E5})$$

The force acting on each polarized particle can be divided into two parts. The first term is the same on both sides of the interferometer arm, while the second term differs due to the

spatial superposition state of the diamond. It should be noted that  $F_i$  here represents the force experienced by each polarized atom, and depending on their equilibrium positions, the force on each atom is different. However, since in this model  $X_{i+1} - X_i = \text{const}$ , where  $\text{const}$  represents the distance between two atoms, we have  $X_i^L - X_i^R = \Delta X_c$ . Substituting (E5) into (26) and (27), one can obtain the contrast loss caused by the induced dipole-phonon interaction as

$$C_{\text{dp}} = \prod_q \exp \left( - \frac{\coth \frac{1}{2} \frac{\hbar \omega_q}{k_B T}}{\hbar \omega_q} \left| \frac{3V \Delta X_m \eta_e^2 \epsilon_0 (\epsilon_r - 1)}{\tau_a^2 \omega_q^3 \epsilon_r (\epsilon_r + 2)} \Gamma(\omega_q) \right|^2 \right), \quad (\text{E6})$$

where  $\Gamma(\omega_q)$  is related to the Fourier transform given in (30). Here one can estimate that the contrast loss induced by the induced dipole is very weak. Taking the diamond masses of interest ( $10^{-20}$ – $10^{-14}$  kg) as an example, their phonon frequency ranges from tens of gigahertz to several terahertz. In this case, the first term in (E6) is approximately of magnitude of  $10^{-24}$ . For the absolute value term, even if one chooses the maximum value of  $\Gamma(\omega_q)$  and specifies a splitting protocol that achieves a maximum splitting of around  $100 \mu\text{m}$  within 1 s, the order of magnitude of this term only reaches about  $10^{-130} \eta_e^4$ . Consider a case where a single charge is held at a distance of  $500 \mu\text{m}$  away from the diamond. In this case the electric-field gradient reaches only  $30 \text{ V/m}^2$ . Even if one assumes that the distance between the free charge held from the diamond reaches  $100 \text{ nm}$ , the electric-field gradient at this point is approximately  $10^{10} \text{ V/m}^2$ , which is not sufficient to increase the contrast caused by dipole–electric-field–phonon coupling, which becomes negligible.

- 
- [1] R. Penrose, *Gen. Rel. Grav.* **28**, 581 (1996).  
[2] L. Diósi, *Phys. Rev. A* **40**, 1165 (1989).  
[3] P. M. Pearle, *Phys. Rev. A* **39**, 2277 (1989).  
[4] A. Bassi, K. Lochan, S. Satin, T. P. Singh, and H. Ulbricht, *Rev. Mod. Phys.* **85**, 471 (2013).  
[5] S. Nimmrichter and K. Hornberger, *Phys. Rev. Lett.* **110**, 160403 (2013).  
[6] C. Overstreet, P. Asenbaum, T. Kovachy, R. Notermans, J. M. Hogan, and M. A. Kasevich, *Phys. Rev. Lett.* **120**, 183604 (2018).  
[7] P. Asenbaum, C. Overstreet, M. Kim, J. Curti, and M. A. Kasevich, *Phys. Rev. Lett.* **125**, 191101 (2020).  
[8] S. Bose, A. Mazumdar, M. Schut, and M. Toroš, *Entropy* **25**, 448 (2023).  
[9] S. Chakraborty, A. Mazumdar, and R. Pradhan, *Phys. Rev. D* **108**, L121505 (2023).  
[10] O. Romero-Isart, *Phys. Rev. A* **84**, 052121 (2011).  
[11] O. Romero-Isart, A. C. Pflanzer, F. Blaser, R. Kaltenbaek, N. Kiesel, M. Aspelmeyer, and J. I. Cirac, *Phys. Rev. Lett.* **107**, 020405 (2011).  
[12] O. Romero-Isart, M. L. Juan, R. Quidant, and J. I. Cirac, *New J. Phys.* **12**, 033015 (2010).  
[13] J. Tilly, R. J. Marshman, A. Mazumdar, and S. Bose, *Phys. Rev. A* **104**, 052416 (2021).  
[14] M. Schut, J. Tilly, R. J. Marshman, S. Bose, and A. Mazumdar, *Phys. Rev. A* **105**, 032411 (2022).  
[15] T. W. van de Kamp, R. J. Marshman, S. Bose, and A. Mazumdar, *Phys. Rev. A* **102**, 062807 (2020).  
[16] S. Rijavec, M. Carlesso, A. Bassi, V. Vedral, and C. Marletto, *New J. Phys.* **23**, 043040 (2021).  
[17] F. Gunnink, A. Mazumdar, M. Schut, and M. Toroš, *Class. Quantum Grav.* **40**, 235006 (2023).  
[18] M. Schut, H. Bosma, M. Wu, M. Toroš, S. Bose, and A. Mazumdar, *Phys. Rev. A* **110**, 022412 (2024).  
[19] P. Fragolino, M. Schut, M. Toroš, S. Bose, and A. Mazumdar, *Phys. Rev. A* **109**, 033301 (2024).  
[20] M. Toroš, A. Mazumdar, and S. Bose, *Phys. Rev. D* **109**, 084050 (2024).  
[21] M. Schut, A. Grinin, A. Dana, S. Bose, A. Geraci, and A. Mazumdar, *Phys. Rev. Res.* **5**, 043170 (2023).  
[22] R. J. Marshman, A. Mazumdar, G. W. Morley, P. F. Barker, S. Hoekstra, and S. Bose, *New J. Phys.* **22**, 083012 (2020).  
[23] E. Kilian, M. Toroš, F. F. Deppisch, R. Saakyan, and S. Bose, *Phys. Rev. Res.* **5**, 023012 (2023).  
[24] P. F. Barker, S. Bose, R. J. Marshman, and A. Mazumdar, *Phys. Rev. D* **106**, L041901 (2022).  
[25] A. Peters, K. Y. Chung, and S. Chu, *Nature (London)* **400**, 849 (1999).

- [26] R. Y. Chiao and A. D. Spiliotopoulos, *J. Mod. Opt.* **51**, 861 (2004).
- [27] A. Roura, D. R. Brill, B. L. Hu, C. W. Misner, and W. D. Phillips, *Phys. Rev. D* **73**, 084018 (2006).
- [28] S. Foffa, A. Gasparini, M. Papucci, and R. Sturani, *Phys. Rev. D* **73**, 022001 (2006).
- [29] S. Dimopoulos, P. W. Graham, J. M. Hogan, M. A. Kasevich, and S. Rajendran, *Phys. Rev. D* **78**, 122002 (2008).
- [30] S. Dimopoulos, P. W. Graham, J. M. Hogan, M. A. Kasevich, and S. Rajendran, *Phys. Lett. B* **678**, 37 (2009).
- [31] G. M. Tino *et al.*, *Eur. Phys. J. D* **73**, 228 (2019).
- [32] P. W. Graham, J. M. Hogan, M. A. Kasevich, and S. Rajendran, *Phys. Rev. Lett.* **110**, 171102 (2013).
- [33] M.-Z. Wu, M. Toroš, S. Bose, and A. Mazumdar, *Phys. Rev. D* **107**, 104053 (2023).
- [34] S. Bose, A. Mazumdar, G. W. Morley, H. Ulbricht, M. Toroš, M. Paternostro, A. A. Geraci, P. F. Barker, M. S. Kim, and G. Milburn, *Phys. Rev. Lett.* **119**, 240401 (2017).
- [35] D. Biswas, S. Bose, A. Mazumdar, and M. Toroš, *Phys. Rev. D* **108**, 064023 (2023).
- [36] F. Hanif, D. Das, J. Halliwell, D. Home, A. Mazumdar, H. Ulbricht, and S. Bose, [arXiv:2307.08133](https://arxiv.org/abs/2307.08133).
- [37] R. J. Marshman, A. Mazumdar, and S. Bose, *Phys. Rev. A* **101**, 052110 (2020).
- [38] S. Bose, A. Mazumdar, M. Schut, and M. Toroš, *Phys. Rev. D* **105**, 106028 (2022).
- [39] U. K. B. Vinckers, Á. de la Cruz-Dombriz, and A. Mazumdar, *Phys. Rev. D* **107**, 124036 (2023).
- [40] S. G. Elahi and A. Mazumdar, *Phys. Rev. D* **108**, 035018 (2023).
- [41] M. Christodoulou, A. Di Biagio, M. Aspelmeyer, Č. Brukner, C. Rovelli, and R. Howl, *Phys. Rev. Lett.* **130**, 100202 (2023).
- [42] D. Carney, P. C. E. Stamp, and J. M. Taylor, *Class. Quantum Grav.* **36**, 034001 (2019).
- [43] D. L. Danielson, G. Satishchandran, and R. M. Wald, *Phys. Rev. D* **105**, 086001 (2022).
- [44] C. H. Bennett, D. P. DiVincenzo, J. A. Smolin, and W. K. Wootters, *Phys. Rev. A* **54**, 3824 (1996).
- [45] B. Friedrich and H. Schmidt-Böcking, *Molecular Beams in Physics and Chemistry: From Otto Stern's Pioneering Exploits to Present-Day Feats* (Springer International Publishing, Cham, 2021), pp. 37–88.
- [46] S. Machluf, Y. Japha, and R. Folman, *Nat. Commun.* **4**, 2424 (2013).
- [47] Y. Margalit, O. Dobkowski, Z. Zhou, O. Amit, Y. Japha, S. Mouskouri, D. Rohrlich, A. Mazumdar, S. Bose, C. Henkel, and R. Folman, *Sci. Adv.* **7**, eabg2879 (2021).
- [48] M. Schut, A. Geraci, S. Bose, and A. Mazumdar, *Phys. Rev. Res.* **6**, 013199 (2024).
- [49] E. Joos, H. D. Zeh, C. Kiefer, D. Giulini, J. Kupsch, and I.-O. Stamatescu, *Decoherence and the Appearance of a Classical World in Quantum Theory* (Springer, Berlin, 2003).
- [50] M. Schlosshauer, *Phys. Rep.* **831**, 1 (2019).
- [51] R. J. Marshman, A. Mazumdar, R. Folman, and S. Bose, *Phys. Rev. Res.* **4**, 023087 (2022).
- [52] R. J. Marshman, S. Bose, A. Geraci, and A. Mazumdar, *Phys. Rev. A* **109**, L030401 (2024).
- [53] M. Toroš, T. W. Van De Kamp, R. J. Marshman, M. S. Kim, A. Mazumdar, and S. Bose, *Phys. Rev. Res.* **3**, 023178 (2021).
- [54] A. Großardt, *Phys. Rev. A* **102**, 040202(R) (2020).
- [55] B. Englert, J. Schwinger, and M. O. Scully, *Found. Phys.* **18**, 1045 (1988).
- [56] J. Schwinger, M. O. Scully, and B. G. Englert, *Z. Phys. D* **10**, 135 (1988).
- [57] M. O. Scully, B.-G. Englert, and J. Schwinger, *Phys. Rev. A* **40**, 1775 (1989).
- [58] B.-G. Englert, *Z. Naturforsch. A* **52**, 13 (1997).
- [59] Y. Japha and R. Folman, *Phys. Rev. Lett.* **130**, 113602 (2023).
- [60] C. Henkel and R. Folman, *AVS Quantum Sci.* **4**, 025602 (2022).
- [61] C. Henkel and R. Folman, [arXiv:2305.15230](https://arxiv.org/abs/2305.15230).
- [62] R. Zhou, R. J. Marshman, S. Bose, and A. Mazumdar, *Phys. Scr.* **99**, 055114 (2024).
- [63] R. Zhou, R. J. Marshman, S. Bose, and A. Mazumdar, *Phys. Rev. Res.* **4**, 043157 (2022).
- [64] R. Zhou, R. J. Marshman, S. Bose, and A. Mazumdar, *Phys. Rev. A* **107**, 032212 (2023).
- [65] R. A. Jishi, *Feynman Diagram Techniques in Condensed Matter Physics* (Cambridge University Press, Cambridge, 2013).
- [66] N. N. Greenwood and A. Earnshaw, *Chemistry of the Elements* (Elsevier, Amsterdam, 2012).
- [67] W. B. Case, *Am. J. Phys.* **76**, 937 (2008).
- [68] T. Delord, P. Huillery, L. Nicolas, and G. Hétet, *Nature (London)* **580**, 56 (2020).
- [69] M. Perdriat, C. Pellet-Mary, P. Huillery, L. Rondin, and G. Hétet, *Micromachines* **12**, 651 (2021).
- [70] R. O'Handley, *Modern Magnetic Materials: Principles and Applications* (Wiley, New York, 1999).
- [71] J. Heremans, C. H. Olk, and D. T. Morelli, *Phys. Rev. B* **49**, 15122 (1994).
- [72] C. Henkel, G. Jacob, F. Stopp, F. Schmidt-Kaler, M. Keil, Y. Japha, and R. Folman, *New J. Phys.* **21**, 083022 (2019).
- [73] H. J. Mamin, C. T. Rettner, M. H. Sherwood, L. Gao, and D. Rugar, *Appl. Phys. Lett.* **100**, 013102 (2012).
- [74] C. Gonzalez-Ballester, D. Hümmer, J. Gieseler, and O. Romero-Isart, *Phys. Rev. B* **101**, 125404 (2020).
- [75] C. Kittel and P. McEuen, *Introduction to Solid State Physics* (Wiley, New York, 2018).